Published in final edited form as:
Anal Chem. 2014 January 21; 86(2): 1067–1075. doi:10.1021/ac402603j.

Examining the Interactions of the Splicing Factor MBNL1 with Target RNA Sequences via a Label-Free, Multiplex Method

Amrita R. Yadav[†], **Charles R. Mace**[§], and **Benjamin L. Miller**[§,‡,⊥,*]

[†]Department of Physics and Astronomy, University of Rochester, Rochester, NY 14627

[§]Department of Biochemistry and Biophysics, University of Rochester, Rochester, NY 14642

[‡]Department of Biomedical Engineering, University of Rochester, Rochester, NY 14627

[⊥]Department of Dermatology, University of Rochester, Rochester, NY 14642

Abstract

The near-ubiquity of the involvement of RNA in crucial biological processes is accepted. It is important, therefore, to study and understand the biophysical principles that regulate the function of RNA and its interactions with other molecules (e.g., proteins and antibiotics). Methods enabling the high-throughput determination of RNA–protein binding kinetics and thermodynamics would greatly accelerate understanding of these interactions. To that end, we describe the development of a real-time biomolecular interaction analysis platform based on arrayed imaging reflectometry (AIR) for multiplex analysis of RNA–protein interactions. We demonstrate the use of aqueous AIR by measuring the binding kinetics between muscleblind-like 1 (MBNL1), a splicing regulator protein that plays a pivotal role in the Myotonic Dystrophies and Huntington's Disease, and several of its RNA targets simultaneously on a microarrayed chip. Using this approach, we observe that the kinetics of MBNL1 binding isolated CUG and repeat CUG RNA sequences (as models for “normal” and “pathogenic” RNA, respectively) are different even though their steady state binding constants are similar. The ability to compare binding kinetics between RNA sequences rapidly and easily may provide insight into the molecular basis of MBNL1-RNA binding, and more generally suggests that AIR can be a powerful tool to enable the label-free, real-time analysis of biomolecular interactions in a high throughput format.

Keywords

Label-free; multiplex; binding kinetics; MBNL1; RNA; biosensor; Arrayed Imaging Reflectometry

INTRODUCTION

RNA is a fundamental component of the flow of biological information: transcription, translation, and regulation of gene expression.[1] This wide range of functions is achieved due to the ability of RNA to fold into three-dimensional structures that can interact selectively with other molecules.[2] Often, these interactions are implicated in diseases, and a thorough

[*]**Corresponding Author** Benjamin L. Miller Department of Dermatology University of Rochester 575, Elmwood Avenue, Rochester, NY 14642. Benjamin_miller@urmc.rochester.edu Phone number: 585-275-9805.

Supporting Information. Supplemental figures and tables referred to in the text and detailed experimental and data analysis methods. This material is available free of charge via the Internet at http://pubs.acs.org.

Author Contributions The manuscript was written through contributions of all authors. All authors have given approval to the final version of the manuscript.

understanding of them is crucial for the development of potential therapeutics. One such disease-state interaction involves the protein muscleblind-like 1 (MBNL1), an alternative-splicing regulator that is important for terminal muscle differentiation.[3] Aberrations in its function play a central role in several neurodegenerative disorders, which include Myotonic Dystrophy types 1 and 2 (DM1 and DM2) and Huntington's Disease (HD).[4,5] These disorders are characterized by a genetic mutation where typically short tri- or tetra-nucleotide repeat sequences (≤ 40 repeats) are expanded to very long repeats (hundreds to thousands of nucleotides).[5] The high affinity of MBNL1 to these repeat sequences results in its sequestration in large protein- RNA clusters known as foci, and splicing misregulation of several genes, thus causing disease.[4,5] The disruption of MBNL1–RNA interactions has been shown to restore normal splicing regulation and reverse disease symptoms in DM1 and HD.[6,7,8] Efforts to develop ligands targeting the RNA expansions responsible for DM2 are in progress,[9,10,11] and disruption of the interactions between mutant RNA transcripts and MBNL1 is recognized as a promising therapeutic goal. A thorough characterization of these interactions can be helpful in the efficient design and development of drugs targeting them.

Conventional methods for studying RNA–protein interactions (e.g., assays based on electrophoretic mobility shift, nitrocellulose filter binding, fluorescence polarization, isothermal titration calorimetry, equilibrium dialysis, and UV crosslinking)[12] involve steady-state analysis and provide only thermodynamic information. While these data are obviously important, they are also obviously only a part of the overall picture. Along with the affinity constant, kinetic constants of binding are needed to complete the description of a biomolecular interaction. In a cellular environment where many competing interactions occur simultaneously, the biological effect of an interaction often depends on the rapidity of complex formation or on the longevity of the formed complex.[13,14] In the context of protein binding, the dissociation rate (or, equivalently, residence time) has been recognized as an important parameter in the design of drugs with good efficacy and selectivity; drugs with a longer residence time typically are more effective ligands for a target.[15,16] In conjunction with structural information, kinetic studies can also reveal the mechanism of binding for interactions.[17,18] Thus, the elucidation of binding kinetics can provide insights on the specificity, the mechanism, and the biological repercussions of an interaction.

The determination of binding kinetics requires monitoring in real time. The use of labels or secondary reagents, typical strategies used by a number of methods, risks modifying the tertiary structure of one or both of the molecules under study and/or altering the interaction kinetics. Label-free methods for biomolecular interaction analysis are, therefore, essential. Towards this end, many techniques have been developed based on the optical,[19,20,21] plasmonic,[22] mechanical[23] or electrical[24] properties of materials. Perhaps the most familiar of these is surface plasmon resonance (SPR) spectroscopy, which allows measurement of biomolecular binding kinetics. However, SPR spectroscopy is limited to monitoring a few interactions simultaneously (as far as we are aware, the maximum number available in a currently available commercial instrument is 36)[25]. Extension of the SPR technique to a high-throughput imaging platform results in a greatly reduced detection sensitivity,[22] or requires complicated instrumentation and experimental methods.[26,27,28] Other recently developed microfluidics-based methods have been useful in obtaining multiplexed kinetic measurements,[29] but the complexity of the device format and the necessity of labeled probes suggest that simpler alternatives are desirable. Thus, there is still an unmet need for a real-time method for the determination of binding kinetics that is easily multiplexed while retaining high sensitivity and a simple instrument design.

To address this gap, we have developed arrayed imaging reflectometry (AIR), an optical technique based on the creation and binding-based destruction of a near-perfect condition of anti-reflectance.[30,31] The AIR technique is sensitive to sub-Ångstrom changes in the local

thickness of a thin film, and the imaging-based method of detection (using a CCD camera) is amenable to high-throughput applications. We have previously demonstrated the utility of AIR for the exceptionally sensitive multiplexed detection of peptides,[31] proteins,[32,33] and antibodies[34] and have shown that the performance of AIR is a predictable function of the size and binding properties of the probe and target molecules across a range of probe–target affinities.[35] Thermodynamic affinities (K_D) measured for several binding pairs were found to be in good agreement with those obtained using SPR or isothermal titration calorimetry (summarized in Supporting Information, S17). However, all previous results have been in an end-point format (substrates were washed and dried at the end of the experiment and imaged under air) and consequently precluded kinetic analysis.

In this article, we develop a version of AIR suitable for measurement under aqueous media, which enables reflectance data to be monitored in real-time for the elucidation of biomolecular binding kinetics over an array. We demonstrate this approach by measuring the binding kinetics of MBNL1 to several RNA sequences microarrayed on an AIR chip. The steady-state affinities of some of these interactions have been reported previously; however, to the best of our knowledge, their kinetic binding parameters are not known. Our results using this method suggest that the kinetic rate constants can differentiate between RNA sequences that have similar thermodynamic affinities towards MBNL1. These differences may provide useful information regarding the sequestration of MBNL1 by mutant RNA expansions.

EXPERIMENTAL SECTION

Substrate fabrication, characterization and reflectance calculations

The substrate used for aqueous AIR experiments is a bilayer stack consisting of layers of silicon nitride (~89 nm thick) and silicon dioxide (~230 nm thick) on top of a silicon chip (Figure 1a) (see Supporting Information for fabrication details). The reflectance of the silicon nitride/silicon dioxide structure was calculated using a standard matrix method used for multilayered thin films.[36] Each layer was represented by a 2 × 2 matrix, which contained information about the thickness, refractive index and the angle of propagation of light through the layer. The nitride and oxide layer refractive indices were characterized using spectroscopic ellipsometry (see Supporting Information for details). The refractive index of biomaterial on top of the oxide layer was approximated to be the same as the oxide layer.[21] Matrices for the different layers of the AIR chip were multiplied to get a final characteristic matrix for the entire structure which was used to calculate the reflectance of the structure.

Sensor chip preparation

10 mm × 10 mm chips diced from substrate wafers were etched and functionalized with aminopropyl dimethyl ethoxysilane (APDMES) and glutaraldehyde (see Supporting Information for details). All RNA sequences were obtained from a commercial source with biotin conjugated to the 5′ terminus to facilitate immobilization via streptavidin capture. RNA sequences were heated to their respective melting temperatures at a concentration of 26.6 μM and cooled before immobilization to ensure correct folding. Biotinylated RNA was incubated with streptavidin for 60 minutes before microarraying on the chips. Spots containing streptavidin alone and two concentrations of biotinylated bovine serum albumin (BSA) (10 and 20 μg/mL, BSA-10 and BSA-20) incubated with streptavidin were printed as references for background subtraction and reflectance-to-thickness conversion, respectively. Combined with examination of the chip surface itself, these also permit evaluation of nonspecific binding. After RNA immobilization, the remaining aldehyde groups and biotin-binding sites on streptavidin were blocked with BSA and biotin, respectively.

Optical and flow set-up

The chip reflectance was monitored using a simple optical setup (Figure 1b). The light from a linearly polarized HeNe laser (632.8 nm wavelength) was collimated and passed through a Glan-Thompson polarizer, which enforced a measured 50000:1 s:p polarization purity. The beam was expanded before being incident on the chip in a custom flow cell mounted on a rotation stage to adjust the angle of incidence. A right-angled prism coupled light into and out of the flow cell, and also acted as the seal for the flow cell. The chip was mounted onto an angled wedge (3°) in order to minimize secondary interference effects from the face of the prism. The reflected beam from the chip was imaged onto a Sony XCD-SX910 CCD camera. All images and videos were acquired using AstroIIDC software (Version 3.02.03, Aupperle Services and Contracting). Videos were acquired at 3 frames per minute at integration times of 75 – 250 ms. A dark frame image with the reflection of the chip blocked from the sensor was acquired with each experiment.

Binding experiments

MBNL1 was expressed and purified from bacterial cultures (details in Supporting Information). Prepared chips were mounted into the flow cell (Figure 1b); solutions were introduced into the cell via a luer inlet port using a syringe pump (NE-1000, New Era Pump Systems Inc., Farmington, NY) and eluted solutions were removed through a similar outlet port. The volume of the flow cell was ~400 μL.

AIR binding studies were performed at a flow rate of 400 μL/min in a running buffer consisting of MPBS-ET-200 (10 mM NaH_2PO_4, 10 mM Na_2HPO_4, 200 mM NaCl, 3 mM EDTA, 2 mM $MgCl_2$ and 0.005% Tween-20, pH 7.2) supplemented with 300 μg/mL BSA as a carrier protein. 6 mL of MBNL1 (100 – 250 nM concentration) was injected over the chip for a 15-minute association phase, followed by a ~25 minute dissociation under buffer flow. The sensor surface was regenerated using an aqueous solution containing 5 mM NaOH and 450 mM NaCl (pH 11.4) (see Supporting Information for discussion of RNA stability under these regeneration conditions). Detailed procedures for the SPR binding experiments can be found in Supporting Information.

Data analysis

The association and dissociation phase videos were converted into image sequences and analyzed using ImageJ.[37] The average intensity of each spot was measured as a function of time after subtracting the intensity of the dark frame image. The reflected intensity values were then converted into thickness values as described in SI text. The thickness of material accumulated on streptavidin spots was subtracted from that of all other RNA spots. The reference-subtracted binding curves were fit to a 1:1 Langmuir binding model using Scrubber2 (BioLogic Software, Pty., Australia) to obtain the association and dissociation rates (k_a and k_d, respectively) and the dissociation constant (K_D). Statistical analysis to compare affinity and kinetic constants of RNA sequences was performed using one-way Anova followed by a Tukey-Kramer *post hoc* test (Matlab).

RESULTS AND DISCUSSION

Detection mechanism

The basic principle of AIR has been described in detail elsewhere.[31] In brief, we use a thin layer of thermally grown silicon dioxide to create a near-perfect anti-reflective coating on the surface of a silicon substrate (a “chip”) for a particular state of incident light (s-polarized light at 632.8 nm, incident at an angle of 70.7°). This condition of minimum reflectivity is highly sensitive to the thickness of the anti-reflective coating, which can comprise an arrayed layer of biomolecular probes in addition to a base layer of silicon dioxide. Binding

of a target molecule results in an increase in the local thickness of the probe layer; this increase in thickness causes an increase in reflectance that can be quantified using a simple imaging apparatus.

Aqueous AIR substrate

The silicon-silicon dioxide chip used for dry (i.e., endpoint) AIR assays satisfies the minimum reflectivity condition in an aqueous medium only at grazing angles of incidence (~ 85°) that are difficult to achieve experimentally. Enabling aqueous AIR detection at a reasonable angle required the use of a coating with a higher refractive index than silicon dioxide. For this purpose, we used a silicon/silicon nitride/silicon dioxide stack[38] (Figure 1a) as the substrate of choice because of (i) the existence of well-characterized, cost-effective deposition methods for these materials,[39,40] (ii) the ability to control the thickness of the top silicon dioxide layer using dilute hydrofluoric acid etching with sub-Ångstrom precision,[41] and (iii) the wide range of immobilization chemistries for probe molecule attachment compatible with the top silicon dioxide surface.[42]

Calculations based on the transfer matrix formalism for multilayer coatings[36] showed that for s-polarized light at a wavelength of 632.8 nm, the minimum reflectivity condition is satisfied at a silicon nitride thickness of 90 nm, silicon dioxide thickness of 230 nm and an angle of incidence of 52.35° with water as the ambient medium. Simulation of the reflectance (Figure 1c) of the sensor chip as a function of these conditions (black dotted line) shows that the sensor surface is nearly anti-reflective: less than 1 part-per-billion of the incident optical power is reflected. The reflectance of the sensor increases as 0.2 nm (red lines), 0.5 nm (blue lines) and 1 nm (green lines) of biomaterial—assumed to have the same refractive index as silicon dioxide—is added. In total, the calculated reflectance increases by 1.2×10^4-fold upon addition of 1 nm of biomaterial.

The thickness of the intermediate silicon nitride layer and major variations in the refractive index of the ambient solution (e.g., n = 1.336 for a solution with 200 mM NaCl instead of n = 1.333 for water) affect the minimum reflectance condition but can be compensated for by changing the oxide thickness and the angle of incidence as required for minimum reflectance (Figure S1, Supporting Information). The thickness of the silicon dioxide layer can be controlled precisely via dilute hydrofluoric acid etching;[41] the angle of incidence can be adjusted easily by mounting the chip on a rotation stage.

Using this device, we observe a clear contrast in images acquired from a chip with circular posts of 1 nm height patterned in the layer of silicon dioxide (Figures 1d and 1e). Detectable contrasts are observed for post heights as small as 1 Ångstrom. Two primary factors currently limit the experimental sensitivity from approaching that suggested by simulations: (i) The light beam used to image the chip has a ~50000:1 s- to p-polarization ratio. The presence of a small amount of p-polarized light makes the reflectivity dip shallower than that expected for pure s-polarized light, resulting in a smaller reflectance change upon an increase in thickness. (ii) There is ~5% variation in the thicknesses of the deposited silicon nitride and silicon dioxide layers across the 6-inch wafers, and this thickness gradient is observed across single chips (ca. Ångstroms/cm). Since the thinnest region of the chip is designed to satisfy the minimum-reflectivity condition, higher reflected intensities are obtained from the thicker regions of the chip and sensitivity is reduced. Improvements in the polarization purity of the light and the substrate thickness uniformity can therefore improve the detection sensitivity further.[43]

The substrate materials in the aqueous AIR chip have low thermo-optic coefficients, and the sensitivity of the thickness measurements upon target binding is therefore independent of temperature fluctuations. This is a significant advantage over other label-free optical sensing

techniques (e.g., the optical effect monitored in SPR has a strong dependence on temperature).[19,44] To confirm this experimentally, we measured the relationship between the temperature of the medium and the reflectance intensity using a chip patterned with 1 nm posts. We observed a minimal change (~ 0.17 units/°C, corresponding to an apparent ~ 0.05 Å/°C increase) in the background-subtracted reflectance of the posts over a range of temperatures spanning 20 °C (Figure S2, Supporting Information). This insensitivity to the temperature of the ambient medium eliminates temperature-related signal drifts that can be detrimental to the quality of the biosensor data. The background-subtracted signal obtained from aqueous AIR is also independent of minor variations in the refractive index of the bulk medium caused by typical concentrations of analytes in solution (up to 1% sucrose, Figure S2, Supporting Information). Thus, we conclude that the reflectance changes observed from AIR chips are a result of actual biomolecular accumulation on the surface and not environmental factors.

RNA sequence selection

We examined the ability of aqueous AIR to determine RNA-protein binding kinetics in a multiplexed format by printing RNA microarrays consisting of seven RNA sequences onto the chip and then flowing solutions of MBNL1 over them. The RNA sequences and their predicted secondary structures[45] are shown in Figure 2. We selected RNA sequences that have known interactions with MBNL1, well characterized biological roles, and that are known to form stable monomeric hairpins. $(CUG)_n$ and $(CCUG)_n$ are both known to bind MBNL1 with a low- to mid-nanomolar affinity (K_D),[46,47,48,49,50] and are responsible for the pathologies associated with DM1 and DM2, respectively. Previous experiments have shown that the secondary structure of (CUG) repeats is a simple hairpin, and is essentially invariant with repeat length.[51] Thus, $(CUG)_{10}$ and $(CCUG)_{10}$ are widely recognized as effective models for the much larger pathogenic RNAs that cause DM1 and DM2. Two variants of the $(CUG)_n$ repeat, $(CUG)_{10}$ and $(CUG)_2$ were included to test the effect of avidity, if any, on the binding kinetics. As both CUG units in $(CUG)_2$ form a loop and there are no CUG units in the RNA stem (Figure 2), this structure can also provide insight on the role of the loop region in MBNL1 binding. The sequestration of MBNL1 by $(CAG)_n$ is one of the pathologic mechanisms in HD; widely divergent affinities (nanomolar to low micromolar) have been reported for this interaction.[46,48,52] The matched CUG-CAG sequence is not known to be pathogenic, but was included to test the effect of removing all nucleotide mismatches from the RNA hairpin stem, as it has been suggested that MBNL1 prefers to bind GC-rich RNA hairpins with pyrimidine mismatches.[46,47,48] The Tnnt3 SL sequence is a preferred binding site of MBNL1 on the fast skeletal muscle troponin T (Tnnt3) pre-mRNA (a normal splicing target for MBNL1) and has been reported to have an affinity to MBNL1 that is comparable to $(CUG)_n$.[48] A modified RNA sequence derived from the human immunodeficiency virus (HIV)[53] was used as a negative control, as it is not expected to bind MBNL1 specifically.

MBNL1 binding on RNA microarrays

Clear RNA sequence-dependent changes in intensity are readily observed in AIR chip images following exposure to solutions of MBNL1 (Figure 3). The spots in the images appear elliptical because of the oblique angle of incidence (~50°) at which the chip is imaged. A modest amount of probe wash-off effect is visible outside some microarray spots (Figure 3(b)). However, as these artifacts are outside the main spot, they are not considered in the data analysis. Real-time binding data (k_a and k_d) are obtained from image stacks by fitting binding curves generated from the observed thickness accumulation from each spot as a function of time to a 1:1 Langmuir binding model after subtraction of nonspecific binding to the control spots (streptavidin, in these arrays).

Spot-to-spot reproducibility of protein binding on the microarray was tested by printing the $(CUG)_{10}$ RNA sequence in a pattern of five columns with four replicate spots per column. Very similar binding responses were obtained from all 20 spots after 100 nM MBNL1 was introduced into the flow cell (see SI text and Figure S3 for details). This experiment confirmed that the amount of protein bound and its binding kinetics are reproducible across spots and independent of the spot position. The maximum reference-subtracted thickness of MBNL1 bound onto the control HIV-RNA spots was ~0.5 Å, which is just at the limit of detection of our current experiments and cannot be considered significant (Figure S3), particularly compared to the maximum thickness of MBNL1 bound to the other RNA sequences (> 6.5 Å).

Kinetics for RNA-MBNL1 interaction

The repeated nucleotide sequences in the pathogenic RNAs provide multiple potential MBNL1 binding sites. Previous reports have suggested that these interactions are not cooperative for long CUG repeats ($(CUG)_{54}$ or $(CUG)_{90}$).[46,48] Therefore, we assumed that the multiple MBNL1 binding sites on the RNA sequences, if present, were identical with no cooperativity effects, and used a 1:1 Langmuir model to fit the data. This fit the data well, and the use of a more complex model did not improve the fit significantly (Figure S6).

Representative binding curves for the RNA sequences along with their corresponding fits are shown in Figure 4. Each panel in the figure corresponds to a representative spot for one particular RNA sequence, and the four binding curves in the panel correspond to four different concentrations (100, 150, 200 and 250 nM) of MBNL1. The binding rate constants and affinities measured from AIR experiments are reported as averages of a total of n = 10 spots from N = 2 different chips (Table 1). The obtained values of k_a are reproducible with relatively small experimental errors. However, there is a larger deviation in the values of k_d, most likely due to the difficulty of accurately characterizing the slow dissociation phases observed.[54] Improvements in the system stability over longer time periods will allow us to quantify the small decreases in thickness characteristic of slow off-rates and reduce the experimental error. The deviation observed in values for K_D is a direct consequence of the errors in the values for k_d. The affinities of MBNL1 to both model “pathogenic” and “normal” RNA sequences are found to be similar and in the low nanomolar range, and, except for the matched CUG-CAG RNA, fall within the range of literature-reported values for RNA-MBNL1 interactions (Table 1). The disagreement for the matched CUG-CAG RNA relative to literature values is likely due to differences in the RNA sequences and methods used in the reported studies (*vide infra*).[46,47]

The effect of experimental artifacts like steric crowding and analyte rebinding, caused by high surface probe density,[55] was tested by studying the binding kinetics of MBNL1 to RNA using three different RNA spotting concentrations on the chip (10 μM, 20 μM and 40 μM). The measured kinetic constants were consistent and independent of the probe density over the tested range (Figure S5 and Table S1, Supporting Information).

To provide a comparative reference for the affinity and kinetic constants obtained from AIR experiments, we used SPR to examine the binding between MBNL1 and two different RNA sequences, $(CCUG)_{10}$ and matched CUG-CAG. The k_a, k_d and K_D observed for $(CCUG)_{10}$–MBNL1 interaction were $(2.6 \pm 0.3) \times 10^4$ $M^{-1}s^{-1}$, $(2.7 \pm 0.5) \times 10^{-4}$ s^{-1} and (11 ± 3) nM, respectively, and those for CUG-CAG–MBNL1 interaction were $(4.82 \pm 0.01) \times 10^4$ $M^{-1}s^{-1}$, $(4.2 \pm 0.2) \times 10^{-4}$ s^{-1} and (8.7 ± 0.4) nM, respectively. The SPR results confirm that the $(CCUG)_{10}$ and the CUG-CAG RNA sequences used bind MBNL1 with a nanomolar affinity (Figure S7, Supporting Information), consistent with AIR results.

While the thermodynamic affinity constants were in good agreement between SPR and AIR measurements, both the association and dissociation *rates* were faster as measured by SPR. This difference in kinetics could be due to differences in the transport of analyte to the reactive regions: whereas the Biacore X SPR uses a microfluidic flow cell (60 nL volume), flow rates of 50–100 μL/min and a 500 μm × 2400 μm probe surface, the current AIR experiments (400 μL flow cell volume) used a flow rate of 400 μL/min and ~500 μm diameter probe microspots. To confirm this, we modeled the apparent binding kinetics for a reactive microspot in the AIR flow cell geometry (Figure S8, Supporting Information), taking into account the transport of the analyte to the reactive sites via convection and diffusion. We found that the defined association and dissociation rates at the reactive surface (Table S2, Supporting Information) were ~3–3.5-fold and ~1.3-fold faster, respectively, than the observed kinetic rates in the AIR flow cell. Thus, we hypothesize that a large part of the difference in measured kinetic constants (and in particular the association rate) does originate from the different flow geometries. We are currently designing a low-volume flow cell to test this hypothesis in future studies. Differences in immobilization methodology and in the format of the immobilized RNA (planar monolayer in AIR vs. dextran matrix for SPR) may also contribute to differences between the two techniques.

Despite the differences in their absolute values, a central observation is that the rank order of the binding rates for different RNA sequences remains the same irrespective of the method of analysis used: the binding of MBNL1 to CUG-CAG follows faster kinetics than that to $(CCUG)_{10}$ according to both AIR and SPR results. This confirms that the AIR technique can be used reliably to compare the binding kinetics of ligand-analyte pairs in a high-throughput format. In the context of MBNL1-RNA binding, this allows interesting differences between repeat sequences containing U•U mismatches and other sequences to be revealed for the first time.

Figure 5 compares the kinetic constants for MBNL1 binding to all RNA sequences obtained via AIR measurements. The rate constants for MBNL1 binding to $(CUG)_{10}$, $(CCUG)_{10}$ and $(CAG)_{10}$ are almost identical, showing that these interactions are thermodynamically and kinetically very similar. In comparing the binding of MBNL1 to $(CUG)_{10}$ and $(CUG)_2$ RNA, we did not observe any avidity effects; the two RNA sequences had comparable association and dissociation rates. The strong binding of MBNL1 to $(CUG)_2$ on our chips suggests that MBNL1 does bind to loop regions containing CUG units.

We found that CUG-CAG RNA binds MBNL1 with a nanomolar affinity, which is in contrast to previous reports of no or very weak binding due to the absence of nucleotide mismatches in the RNA stem.[46,47] However, the CUG-CAG RNA sequence used in our work does have one CUG and one CAG unit in the loop region (Figure 2). If this loop structure is involved in MBNL1 binding, as the $(CUG)_2$ results and other previously published structural evidence[56] suggest, then one would expect high-affinity binding for CUG-CAG RNA. This also potentially explains why Warf et. al.[46] observed very weak MBNL1 affinity for the CUG-CAG duplex RNA: their RNA sequences had a UUCG tetraloop and no CUG and CAG units in the RNA hairpin loop. Kino et. al.[47] observed that CUG-CAG duplexes did not bind to MBNL1 in a yeast three-hybrid system. However, lack of precise control over environmental conditions and other factors including competitive binding by other cellular constituents can sometimes lead to false negatives in such a system.[57] This is evidenced by their observation of weak and no MBNL1 binding to $(CAG)_n$ and $(CUG)_7$ sequences, respectively, both of which have been shown to bind MBNL1 with a strong affinity in *in vitro* assays.[48,52] Thus, differences in experimental methodology as well as structural differences could have led to contrasting results between our study and some previous reports. A nanomolar *in vitro* affinity of MBNL1 towards CUG-CAG matched RNA was confirmed via our SPR experiments. It should be noted that even though the

affinity between CUG-CAG and MBNL1 is comparable to the other repeat sequences tested in this work, both the on-rates and off-rates for the interaction are ~2-fold faster ($p < 0.01$). Finally, we observed that a normal RNA target for MBNL1, the Tnnt3 SL stemloop, has ~3-fold faster association rate and ~2-fold faster dissociation rate for MBNL1 as compared to the U•U mismatch RNA sequences ($p < 0.01$).

Due to the role of RNA-MBNL1 interactions in human disease, significant research efforts are focused on understanding the mechanism of RNA recognition by MBNL1 and its sequence selectivity. The results of several studies designed to elucidate these interactions have been published.[46,47,48,49,58,59,60] Our study adds a vital characterization parameter of RNA–MBNL1 binding that has been missing from previous studies: information on the binding kinetics *in vitro*. As the multiplexing capability of AIR makes it relatively easy to expand the repertoire of RNA sequences to include other MBNL1 targets, future experiments employing an expanded sequence repertoire will lead to a better understanding of the factors governing MBNL1 binding of RNA, and means to disrupt the interactions for therapeutic purposes.

CONCLUSIONS

The thorough characterization of normal and aberrant protein–RNA interactions provides a basis for understanding the mechanisms of disease states and designing appropriate interventions. Towards this end, we report the development of an enabling analytical technique, aqueous Arrayed Imaging Reflectometry (AIR), which permits the sensitive analysis of biomolecular interactions in a label-free microarray format. To demonstrate the utility of aqueous AIR, we characterized the binding kinetics of the splicing regulator protein MBNL1 with a selection of RNA target sequences as models for “normal” and “pathogenic” binding interactions. We found that models for non-pathogenic sequences had faster association and dissociation rates as compared to models for pathogenic sequences, in spite of very similar binding affinities. This observation may assist in understanding the molecular basis for efficient sequestration of MBNL1 by RNA repeat expansions. Further studies of the MBNL1-RNA interaction will build on these experiments via the use of significantly more complex arrays, incorporating larger numbers of test sequences. Refinement of the instrument design (to enhance sensitivity) and chip chemistry (to further reduce nonspecific binding) is ongoing, and should permit experimentation with lower protein concentrations. We anticipate that the sensitive detection capability, reproducibility, simple and inexpensive implementation, and robustness towards ambient conditions will make AIR a generally useful platform for multiplexed biomolecular interaction analysis.

Supplementary Material

Refer to Web version on PubMed Central for supplementary material.

Acknowledgments

We thank Dr. David Fang for chip refractive index characterization, Dr. Charles Thornton for generous donation of cells expressing MBNL1 and Dr. Christopher Striemer for helpful discussions and assistance in preparing patterned oxide chips. We thank Joe Ciarlei of Sharlay Machine and Fabrication (http://www.sharlaymachine.com) for the fabrication of the flow cell housing. Financial support by the National Institutes of Health (NIGMS grant R01GM100788, NINDS grant 5R21NS071023 and NIH R24-AL054953 via the University of Rochester Human Immunology Center) is gratefully acknowledged. The content is solely the responsibility of the authors and does not necessarily represent the official view of the National Institutes of Health.

ABBREVIATIONS

AIR	Arrayed Imaging Reflectometry
MBNL1	Muscleblind-like 1
SPR	surface plasmon resonance
DM1	Myotonic Dystrophy type 1
DM2	Myotonic Dystrophy type 2
HD	Huntington's Disease.

REFERENCES

(1). Sharp PA. Cell. 2009; 136:577–580. [PubMed: 19239877]

(2). Weeks KM. Curr. Opin. Struct. Biol. 2010; 20:295–304. [PubMed: 20447823]

(3). Pascual M, Vicente M, Monferrer L, Artero R. Differentiation. 2006; 74:65–80. [PubMed: 16533306]

(4). Krzyzosiak WJ, Sobczak K, Wojciechowska M, Fiszer A, Mykowska A, Kozlowski P. Nucleic Acids Res. 2011; 40:11–26. [PubMed: 21908410]

(5). Wojciechowska M, Krzyzosiak WJ. Hum. Mol. Genet. 2011; 20:3811–3821. [PubMed: 21729883]

(6). Wheeler TM, Sobczak K, Lueck JD, Osborne RJ, Lin X, Dirksen R, Thornton CA. Science. 2009; 325:336–339. [PubMed: 19608921]

(7). Warf MB, Nakamori M, Matthys CM, Thornton CA, Berglund JA. Proc. Natl. Acad. Sci. USA. 2009; 106:18551–18556. [PubMed: 19822739]

(8). Kumar A, Parkesh R, Sznajder LJ, Childs-Disney JL, Sobczak K, Disney MD. ACS Chem. Biol. 2012; 7:496–505. [PubMed: 22252896]

(9). Ofori LO, Hoskins J, Nakamori M, Thornton CA, Miller BL. Nucleic Acids Res. 2012; 40:6380–6390. [PubMed: 22492623]

(10). Wong C-H, Fu Y, Ramisetty SR, Baranger AM, Zimmerman SC. Nucleic Acids Res. 2011; 39:8881–8890. [PubMed: 21768123]

(11). Lee MM, Pushechnikov A, Disney MD. ACS Chem. Biol. 2009; 4:345–355. [PubMed: 19348464]

(12). Pagano JM, Clingman CC, Ryder SP. RNA. 2011; 17:14–20. [PubMed: 21098142]

(13). Wu H, Pfarr DS, Tang Y, An L-L, Patel NK, Watkins JD, Huse WD, Kiener PA, Young JF. J. Mol. Biol. 2005; 350:126–144. [PubMed: 15907931]

(14). Kersh GJ, Kersh EN, Fremont DH, Allen PM. Immunity. 1998; 9:817–826. [PubMed: 9881972]

(15). Lu H, Tonge PJ. Curr. Opin. Chem. Biol. 2010; 14:467–474. [PubMed: 20663707]

(16). Phillips DR, Crothers DM. Biochemistry. 1986; 25:7355–7362. [PubMed: 3801418]

(17). Gilbert SD, Stoddard CD, Wise SJ, Batey RT. J. Mol. Biol. 2006; 359:754–768. [PubMed: 16650860]

(18). James LC, Tawfik DS. Proc. Natl. Acad. Sci. USA. 2005; 102:12730–12735. [PubMed: 16129832]

(19). Washburn AL, Gunn LC, Bailey RC. Anal. Chem. 2009; 81:9499–9506. [PubMed: 19848413]

(20). Pal S, Guillermain E, Sriram R, Miller BL, Fauchet PM. Biosens. Bioelectron. 2011; 26:4024–4031. [PubMed: 21524903]

(21). Özkumur E, Needham JW, Bergstein DA, Gonzalez R, Cabodi M, Gershoni JM, Goldberg BB, Ünlü MS. Proc. Natl. Acad. Sci. USA. 2008; 105:7988–7992. [PubMed: 18523019]

(22). Homola J. Chem. Rev. 2008; 108:462–493. [PubMed: 18229953]

(23). Buchapudi KR, Huang X, Yang X, Ji H-F, Thundat T. Analyst. 2011; 1316:1539–1556. [PubMed: 21394347]

(24). Zheng G, Patolsky F, Cui Y, Wang WU, Lieber CM. Nat. Biotechnol. 2005; 23:1294–1301. [PubMed: 16170313]

(25). Bio-Rad ProteOn system. www.bio-rad.com

(26). Ruemmele JA, Golden MS, Gao Y, Cornelius EM, Anderson ME, Postelnicu L, Georgiadis RM. Anal. Chem. 2008; 80:4752–4756. [PubMed: 18476718]

(27). Piliarik M, Vaisocherova H, Homola J. Biosens. Bioelectron. 2005; 20:2104–2110. [PubMed: 15741081]

(28). Halpern AR, Chen Y, Corn RM, Kim D. Anal. Chem. 2011; 83:2801–2806. [PubMed: 21355546]

(29). Einav S, Gerber D, Bryson PD, Sklan EH, Elazar M, Maerkl SJ, Glenn JS, Quake SR. Nat. Biotechnol. 2008; 26:1019–1027. [PubMed: 18758449]

(30). Lu J, Strohsahl CM, Miller BL, Rothberg LJ. Anal. Chem. 2004; 76:4416–4420. [PubMed: 15283581]

(31). Mace CR, Striemer CS, Miller BL. Anal. Chem. 2006; 78:5578–5583. [PubMed: 16878898]

(32). Mace CR, Striemer CS, Miller BL. Biosens. Bioelectron. 2008; 24:334–337. [PubMed: 18599284]

(33). Carter JA, Mehta SM, Mungillo MV, Striemer CC, Miller BL. Biosens. Bioelectron. 2011; 26:3944–3948.

(34). Mace CR, Topham DJ, Mosmann TR, Quataert SA, Treanor JJ, Miller BL. Talanta. 2011; 83:1000–1005. [PubMed: 21147350]

(35). Sriram R, Yadav AR, Mace CR, Miller BL. Anal. Chem. 2011; 83:3750–3757. [PubMed: 21517019]

(36). Hecht, E. Optics. Addison-Wesley; London: 2002. p. 418-420.

(37). Abramoff MD, Magelhaes PJ, Ram SJ. Biophotonics International. 2004; 11:36–42.

(38). Yadav AR, Mace CR, Miller BL. Proc of SPIE. 2011; 7888:78880I-1–78880I-10.

(39). Yota J, Hander J, Saleh AA. J. Vac. Sci. Technol. A. 2000; 18:372–376.

(40). Adams AC, Alexander FB, Capio CD, Smith TE. J. Electrochem. Soc. 1981; 128:1545–1551.

(41). Williams KR, Muller RS. J. Microelectromech. Syst. 1996; 5:256–269.

(42). Jonkheijm P, Weinrich D, Schröder H, Niemeyer CM, Waldmann H. Angew. Chem. Int. Ed. 2008; 47:9618–9647.

(43). The 50,000:1 s- to p-polarization ratio was obtained using a Glan-Thompson polarizer; the ratio can be increased to ~1,000,000:1 by using a thin film polarizer (Semrock, Inc.). While 5–7% thickness uniformity across the wafer is common for state-of-the-art chemical vapor deposition techniques, uniformity over a 1 cm square chip can be improved by using a larger diameter wafer.

(44). Moreira CS, Lima AMN, Neff H, Thirstrup C. Sens. Actuators B Chem. 2008; 134:854–862.

(45). Reuter JS, Mathews DH. BMC Bioinformatics. 2010; 11:129. [PubMed: 20230624]

(46). Warf MB, Berglund JA. RNA. 2007; 13:2238–2251. [PubMed: 17942744]

(47). Kino Y, Mori D, Oma Y, Takeshita Y, Sasagawa N, Ishiura S. Hum. Mol. Genet. 2004; 13:495–507. [PubMed: 14722159]

(48). Yuan Y, Compton SA, Sobczak K, Stenberg MG, Thornton CA, Griffith JD, Swanson MS. Nucleic Acids Res. 2007; 35:5474–5486. [PubMed: 17702765]

(49). Fu Y, Ramisetty SR, Hussain N, Baranger AM. ChemBioChem. 2012; 13:112–119. [PubMed: 22106026]

(50). Arambula JF, Ramisetty SR, Baranger AM, Zimmerman SC. Proc. Natl. Acad. Sci. USA. 2009; 106:16068–16073. [PubMed: 19805260]

(51). Tian B, White RJ, Xia T, Welle S, Turner DH, Mathews MB, Thornton CA. RNA. 2000; 6:79–87. [PubMed: 10668800]

(52). Mykowska A, Sobczak K, Wojciechowska M, Kozlowski P, Krzyzosiak WJ. Nucleic Acids Res. 2011; 39:8938–8951. [PubMed: 21795378]

(53). Palde PB, Ofori LO, Gareiss PC, Lerea J, Miller BL. J. Med. Chem. 2010; 53:6018–6027. [PubMed: 20672840]

54). McDonnell JM. Curr. Opin. Chem. Biol. 2001; 5:572–577. [PubMed: 11578932]

(55). Myszka DG. Curr. Opin. Biotechnol. 1997; 8:50–57. [PubMed: 9013659]

(56). Teplova M, Patel DJ. Nat. Struct. Mol. Biol. 2008; 15:1343–1351. [PubMed: 19043415]

(57). Jaeger S, Eriani G, Martin F. **FEBS** Lett.. 2004; 556:7–12. [PubMed: 14706817]

(58). Goers ES, Purcell J, Voelker RB, Gates DP, Berglund JA. Nucleic Acids Res. 2010; 38:2467–2484. [PubMed: 20071745]

(59). Grammatikakis I, Goo Y-H, Echeverria GV, Cooper TA. Nucleic Acids Res. 2010; 39:2769–2780. [PubMed: 21109529]

(60). García-López A, Llamusi B, Orzáez M, Pérez-Payá E, Artero RD. Proc. Natl. Acad. Sci. USA. 2011; 108:11866–11871. [PubMed: 21730182]

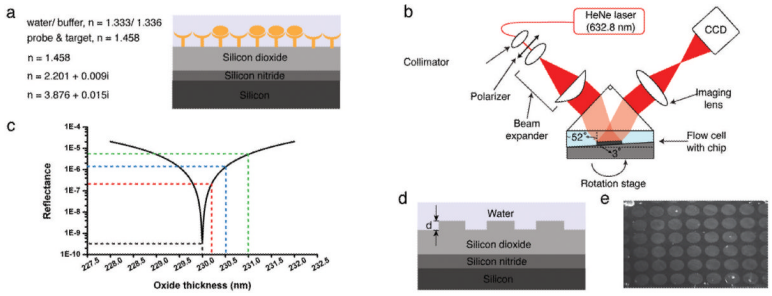

Figure 1.

Aqueous AIR substrate and experimental set-up. (a) Multilayered substrate format for aqueous AIR imaging along with the refractive indices used to measure and/or model the layers (b) Simulated reflectance of the substrate as a function of the thickness of silicon dioxide at a fixed thickness of silicon nitride of 90 nm and angle of incidence of 52.35°. The dashed lines depict the reflectance of the sensor at a starting oxide thickness of 230 nm (black), and its increase as 0.2 nm (red), 0.5 nm (blue) and 1 nm (green) of biomaterial is added on to the sensor surface. (c) Schematic of the experimental set-up used for AIR imaging with target flow experiments. (d) Schematic of a chip with a lithographically patterned layer of silicon dioxide. (e) Aqueous AIR image of a chip depicted in (d) with a post height of 1 nm.

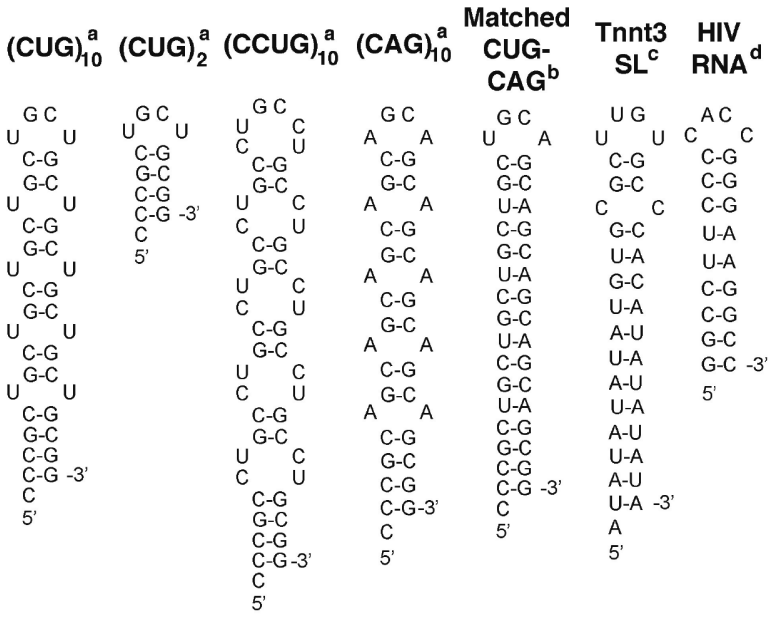

Figure 2.

RNA probe sequences and their secondary structures (modeled using RNAstructure (Ref. 45)). We used seven RNA sequences to measure binding kinetics to MBNL1. (a) Models for pathogenic RNA sequences; (b) Not known to be pathogenic; (c) Normal pre-mRNA target for MBNL1; (d) Negative control RNA sequence.

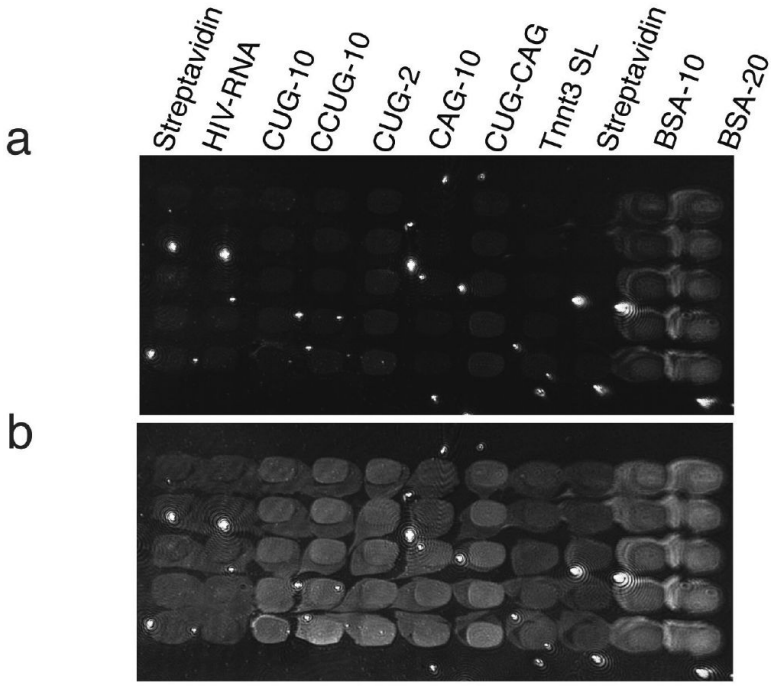

Figure 3.
Images of an RNA microarray acquired using aqueous AIR (a) before and (b) after exposure to 200 nM MBNL1. Each column consists of five replicates of the same spot, and the columns from left to right are as labeled with the sequence. A video of the real-time binding is available (Movie S1).

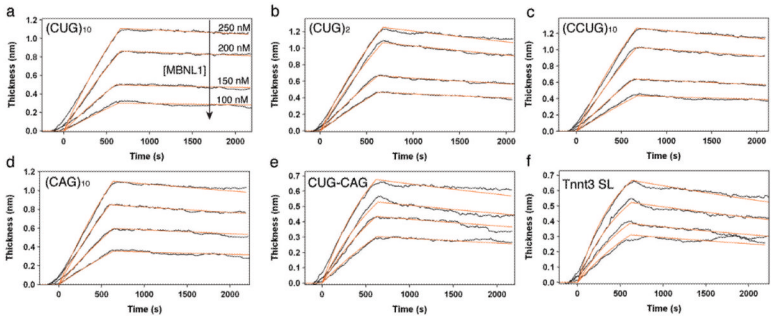

Figure 4.

Representative binding curves obtained from an aqueous AIR microarray experiment and their 1:1 Langmuir model fits. The four binding curves in each panel correspond to four different concentrations of MBNL1 (100, 150, 200, and 250 nM; labeled in the first panel). The black traces represent obtained data and the red traces represent the fit to the data for (a) $(CUG)_{10}$ (b) $(CUG)_2$ (c) $(CCUG)_{10}$ (d) $(CAG)_{10}$ (e) CUG-CAG and (f) Tnnt3 SL.

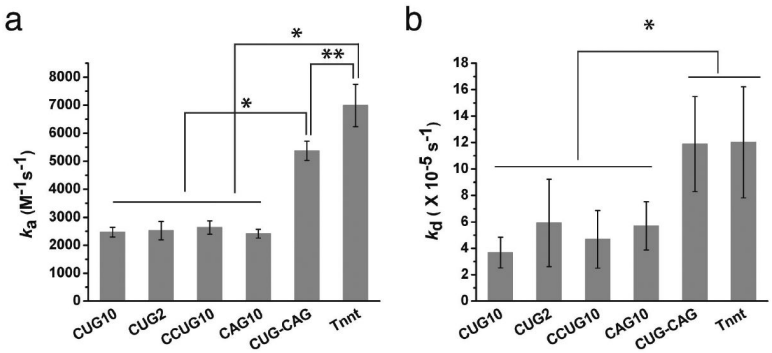

Figure 5.

Kinetic constants for the binding of MBNL1 to different RNA sequences: (a) association rates and (b) dissociation rates. The plotted values are averages over n = 10 spots on N = 2 chips, the error bars represent standard deviation from the mean. Statistical analysis was performed using one-way Anova followed by a Tukey-Kramer *post hoc* test (Matlab). The horizontal lines over groups indicate that there is no significant difference among elements within that group: (*) significantly different from the $(CUG)_{10}$, $(CUG)_2$, $(CCUG)_{10}$ and $(CAG)_{10}$ group; (**) significantly different from CUG-CAG; $p < 0.01$ for both (*) and (**) groups.

Table 1

Rate constants and affinities obtained for RNA sequences using aqueous AIR, and comparison to literature reported affinities

	Aqueous AIR[a]			**Literature reported values**
RNA	k_a ($\times 10^3$ $M^{-1}s^{-1}$)	k_d ($\times 10^{-5}$ s^{-1})	K_D(nM)	K_D(nM)[b]
$(CUG)_{10}$	2.5 ± 0.2	4 ± 1	15 ± 5	4 – 260[c]
$(CUG)_2$	2.5 ± 0.3	6 ± 3	24 ± 13	NR[d]
$(CCUG)_{10}$	2.6 ± 0.2	5 ± 2	18 ± 9	2 – 120[e]
$(CAG)_{10}$	2.4 ± 0.2	6 ± 2	24 ± 8	11 – 1400[f]
CUG-CAG	5.4 ± 0.3[g]	12 ± 4[h]	22 ± 6[i]	11500[j]/ no binding[k]
Tnnt3 SL	7.0 ± 0.8[g,l]	12 ± 4[h]	17 ± 5[i]	7[m]
HIV RNA	No binding	No binding	No binding	NR[d]

[a] Reported values and errors are averages and standard deviations obtained from a total of n = 10 spots from N = 2 experiments.

[b] Values reported for $(CUG)_m$, $(CCUG)_m$ and $(CAG)_m$ where m ranges from 4 to 90, measured using gel shift or filter binding assays, unless otherwise stated.

[c] References 46, 48, 50, 52.

[d] NR: not reported.

[e] References 10, 46, 47.

[f] References 46, 48, 52.

[g] Significantly different ($p < 0.01$) from k_a values for $(CUG)_{10}$, $(CUG)_2$, $(CCUG)_{10}$ and $(CAG)_{10}$.

[h] Significantly different ($p < 0.01$) from k_d values for $(CUG)_{10}$, $(CUG)_2$, $(CCUG)_{10}$ and $(CAG)_{10}$.

[i] Not significantly different ($p > 0.05$) from the K_D values for $(CUG)_{10}$, $(CUG)_2$, $(CCUG)_{10}$ and $(CAG)_{10}$.

[j] Reference 46; value reported for a CUG-CAG duplex with a UUCG tetraloop (see discussion for details).

[k] Reference 47; determined using a yeast three-hybrid system.

[l] Significantly different ($p < 0.01$) from the K_a value for CUG-CAG.

[m] Reference 48 value reported for a 200-nucleotide sequence containing the stemloop. All statistical tests were performed using one-way Anova followed by a Tukey-Kramer *post hoc* test.